Ocean Engineering 363 (2026) 125873

Contents lists available at ScienceDirect

Ocean Engineering

journal homepage: www.elsevier.com/locate/oceaneng

Research paper

Modelling the impact of the foundation shadow effect and flow misalignment disparity on tidal stream turbine performance

Bryn Townley[a,*], Qing Xiao[b], Athanasios Angeloudis[c], Ian Ashton[d], George Dadd[e]

[a] EPSRC and NERC Industrial Centre for Doctoral Training in Offshore Renewable Energy (IDCORE), University of Edinburgh, UK
[b] Naval Architecture, Ocean and Marine Energy, University of Strathclyde, Glasgow, Scotland, UK
[c] Civil and Environmental Engineering, School of Engineering, University of Edinburgh, UK
[d] Department of Engineering, University of Exeter, Penryn, UK
[e] HydroWing, Penryn, Cornwall, UK

ARTICLE INFO

Keywords:
Tidal turbine
Foundation shadowing
Flow misalignment
Load fluctuations
Computational fluid dynamics
Offshore renewable energy

ABSTRACT

Tidal devices in rectilinear flows can utilise bidirectional turbines without the need for an active yawing system. This may improve device reliability by removing active components. However, in this configuration, turbines will experience the 'foundation shadow' effect, as for half of the tidal cycle, they operate in the downstream wake of their own foundation. Additionally, asymmetry between flood and ebb tides is common, causing misalignment between the incoming flow and the turbine rotational axis. This work uses a sliding-mesh unsteady RANS Computational Fluid Dynamics (CFD) model, validated against scale-model and full-scale data, to investigate the severity and implications of the foundation shadow, whilst incorporating flood and ebb asymmetry effects to analyse performance in misaligned flow. The simulations use the HydroWing multi-rotor device and the Tocardo two-bladed Horizontal Axis Tidal Turbine (HATT) as case studies. The use of fairings to streamline the foundation and reduce flow separation is analysed, alleviating the most severe shadowing effects. Results find that for aligned flow, foundation shadowing can induce thrust fluctuations that cause a $\approx 4.6\%$ reduction in mean Power Coefficient (C_P), increasing to $\approx 12.4\%$ when exposed to a yawed inflow. Changing the design by adding a bidirectional fairing to the main support improves the foundation's hydrodynamics, and in turn, reduces the shadowing effect severity to $\approx 2.2\%$ for aligned flow and $\approx 9.7\%$ when misaligned. The structural feasibility of using such a design in a yawed inflow is discussed, and results suggest that turbine yaw misalignment C_P losses are more significant than shadowing at higher angles. Our results demonstrate that by designing for the shadowing effect, the mean C_P impact and magnitude of blade thrust fluctuations can be significantly reduced. For sites with rectilinear tidal cycles, this would enable bidirectional turbines to be used instead of relying on yawing mechanisms.

1. Introduction

Tidal stream device reliability may be improved by utilising a fixed-yaw bidirectional turbine, thus reducing the number of active components required. Fixed yaw turbines in rectilinear tidal flow will operate every other tidal cycle downstream of their foundation, and in this configuration, flow disturbance from the 'foundation shadow' effect can induce cyclic loading, unpredictable turbine performance, and blade fatigue (Larwood and Chow, 2016). Additionally, at most sites, a fixed yaw turbine will experience some degree of misalignment to the incoming tidal flow due to natural asymmetry in flow direction between flood and ebb cycles.

The shadowing effect is more significant for tidal devices than traditional downwind turbines because the monopile tower diameter (D_t) to turbine diameter (D) ratio is higher. As thrust scales with fluid density, tidal turbines typically require larger foundations and smaller diameter turbines to counteract the increased loading. For example, the onshore 5 MW NREL reference wind turbine tower has a D_t that tapers between $0.03D$–$0.05D$ as a ratio of the rotor diameter D, (Jonkman et al., 2009). Whereas for tidal, Frost et al. (2015) and Guo et al. (2020) both modelled 10 m D turbines with larger relative turbine tower diameters that were 0.24 D and 0.2 D respectively.

Guo et al. (2020) showed that monopile shadowing can induce blade fluctuating loads that are 7–8 times greater than in the free stream, and Finnegan et al. (2020) similarly concluded that priority should be given to foundation designs that can minimise shadowing thrust loads. Frost et al. (2015) quantified the losses in mean Power

* Corresponding author.
E-mail address: bryn.townley@ed.ac.uk (B. Townley).

https://doi.org/10.1016/j.oceaneng.2026.125873
Received 6 January 2026; Received in revised form 29 April 2026; Accepted 30 April 2026
Available online 19 June 2026

Coefficient (C_P) due to monopile shadowing to be between 6%–9% depending on clearance distance, and that tidal developers should consider the benefits of using active yawing systems to mitigate the foundation shadowing effect.

However, rather than relying on yawing systems, this study considers alternative design approaches in response to the shadowing effect. We first analyse a multi-rotor structure designed to utilise more favourable D_t/D ratios to reduce the foundation shadow effect, and then consider the effectiveness of symmetrical bidirectional fairings at reducing the foundation shadow effect severity.

We extend the current literature on the foundation shadow effect by considering the additional effects of yaw misalignment, γ, introduced by varying flood and ebb cycles, which are prevalent in tidal sites. Through our latest analysis, we aim to provide developers with practical recommendations for foundation design, helping to improve turbine efficiency and enhance the overall viability of tidal energy projects in rectilinear flow.

1.1. Numerical modelling of the shadowing effect

The influence of the support tower on upstream turbine performance in undisturbed flow has been studied by Mason-Jones et al. (2013) who simulated various tower cross-sectional shapes. Their work showed that an elliptical fairing can reduce thrust loading and the downstream wake profile as compared to a standard cylindrical tubed cross-section. Muchala and Willden (2018) compared the loads along a cylindrical and elliptical tower, showing that foundation cross-sectional shape directly impacts turbine loading and vice versa. They showed that there was an increased velocity deficit upstream and downstream of the support structure for a cylindrical tower compared to the elliptical tower, reducing the blade angle of attack, and thus thrust and torque.

In the wind sector, the shadow effect has primarily been studied for downwind free-yawing turbines. Zahle et al. (2009) simulated the NREL VI turbine behind a monopile foundation and presented load fluctuations along the blades and the tower. Dose et al. (2020) considered the tower shadowing implications for a similar downstream NREL 5 MW wind turbine behind both a cylindrical and a truss monopile foundation. An experimental comparison between an upstream and downstream NREL VI turbine, carried out by Larwood and Chow (2016), showed that downwind operation increased fatigue loading, but this was partially mitigated using a tower shroud aligned with the free-stream flow.

The primary focus of these wind studies was on blade loading and fatigue life rather than power performance, and indeed Larwood and Chow (2016) showed that the energy capture was similar between the upwind and downwind configurations. For tidal, larger relative tower diameters mean that impacts on the turbine C_P are of greater concern, and designing for this may reduce the negative effects of shadowing.

1.2. Case study: HydroWing

The HydroWing multi-rotor concept device mounted with 10 m D Tocardo turbines, Fig. 1, is used as a case study and example of a structure designed, in part, to lower D_t/D ratios. The turbines are non-yawing, fixed-pitch during operation, and feature a passive bi-blade system, whereby the turbine blades pitch 180° about their axis for bidirectional operation. By utilising a truss-like structure, tower diameters are reduced to around 0.06 D, lower than conventional tidal monopile designs.

The horizontal beam, which connects to the turbines, can be seen in red in Fig. 1, and from here on out is referred to as the 'wing'. The wing has a 2:1 oval fairing, and the main structural members are vertical cylindrical tubes with varying diameter ≤ 0.06 D. In Fig. 1(b), we consider a model with a bidirectional fairing, i.e. symmetrical in flood and ebb directions, that has a 0.3 D chord and a 0.1 D thickness, extending from the seabed to the turbine hub.

Previous research has been published investigating various hydrodynamic aspects of the HydroWing device. Smith et al. (2023) modelled the effects of hub spacing and blockage ratio on the performance of two laterally spaced turbines, and analysed the loading increase due to seabed proximity. Then, a preliminary study of this work modelled a simplified multi-rotor device with 0.1 D vertical and horizontal tower diameters to initially analyse the shadowing effect (Townley et al., 2025). Results suggested that with a large D_t/D foundation, the shadowing mean C_P losses could be as much as 10%, prompting this current study to investigate the effectiveness of tower fairings on a lower D_t/D foundation.

2. Methodology

2.1. Governing equations

The Navier–Stokes equations describe fluid motion by defining conservation of mass and momentum. The continuity and momentum equations for incompressible flow can be expressed in the form given by Eqs. (1) and (2) (SIEMENS, 2023).

$$\nabla \cdot \bar{U} = 0 \tag{1}$$

$$\frac{\partial}{\partial t}(\rho \bar{U}) + \nabla \cdot (\rho \bar{U} \otimes \bar{U}) = -\nabla \cdot (\bar{P}\mathbf{I}) + \nabla \cdot (\bar{\mathbf{T}} + \mathbf{T}_{RANS}) + \mathbf{f}_b \tag{2}$$

Where ρ is the fluid density, $\bar{U}$ is the mean velocity, $\bar{P}$ is the mean pressure, $\mathbf{I}$ is the identity tensor, $\bar{\mathbf{T}}$ is the mean viscous stress tensor, $\mathbf{T}_{RANS}$ is a stress tensor, and f_b is the resultant body forces (SIEMENS, 2023).

The RANS turbulence model is widely applied in the tidal industry due to its relative efficiency and accuracy for predicting mean flows. The $k-\omega$ SST transport equations in (3) and (4) are used to close the Navier Stokes equations by calculating k and ω. The SST variant employs the $k-\epsilon$ model in the free stream, and switches to the $k-\omega$ model for near boundary flow by using a blending function.

$$\frac{\partial}{\partial t}(\rho k) + \nabla(\rho k \bar{U}) = \nabla[(\mu + \sigma_k \mu_t)\nabla k] + P_k - \rho\beta^* f_{\beta^*}(\omega k - \omega_0 k_0) + S_k \tag{3}$$

$$\frac{\partial}{\partial t}(\rho \omega) + \nabla(\rho \omega \bar{U}) = \nabla[(\mu + \sigma_\omega \mu_t)\nabla \omega] + P_\omega - \rho\beta f_\beta(\omega^2 - \omega_0^2) + S_\omega \tag{4}$$

Where k is the turbulent kinetic energy, ω is the specific dissipation rate, μ is the dynamic viscosity, σ_k and σ_ω are model coefficients, P_k and P_ω are production terms, f_{β^*} is the free-shear modification factor, f_β is the vortex-stretching modification factor, S_k and S_ω are source terms, and k_0 and ω_0 are the ambient turbulence values that counteract turbulence decay (SIEMENS, 2023).

The Tip Speed Ratio (TSR), C_P, and Thrust Coefficient (C_T) are defined in Eqs. (5)–(7).

$$TSR = \frac{\omega R}{U} \tag{5}$$

$$C_P = \frac{\tau\omega}{0.5\rho A(U)^3} \tag{6}$$

$$C_T = \frac{T}{0.5\rho A(U)^2} \tag{7}$$

where ω is the angular velocity in rad/s, R is the radius in m, U is the free-stream fluid velocity in m/s, τ is the torque in Nm, ρ is the fluid density in kg/m^3, and A is the turbine swept area in m^2.

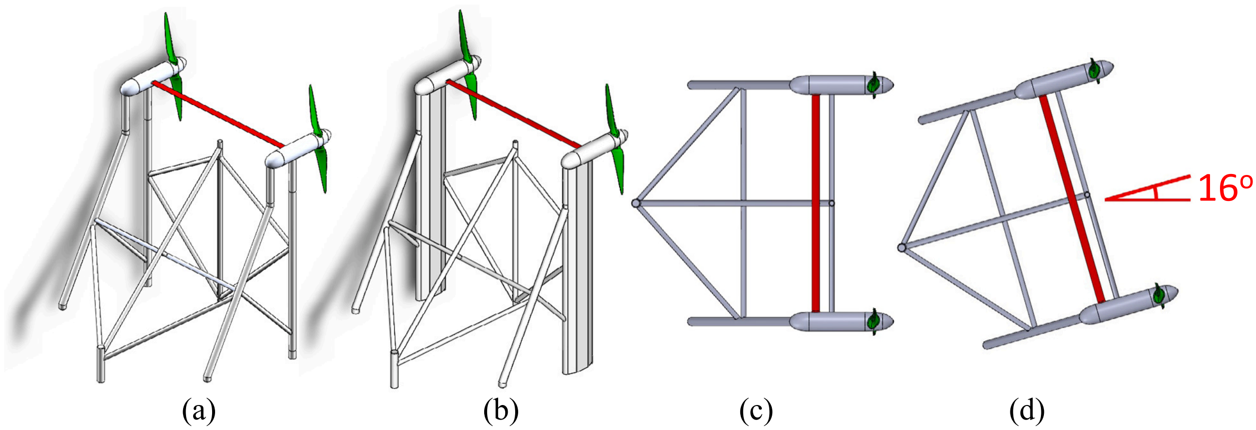

Fig. 1. HydroWing multi-rotor device view. (a) No Fairings (NF). (b) Extended Fairings (EF). (c) Aligned flow. (d) Misaligned flow.

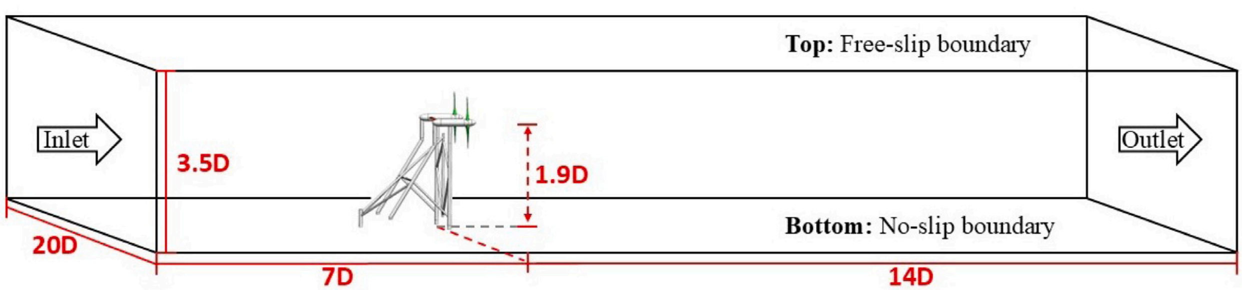

Fig. 2. Domain schematic for the Shadowing Case CFD model.

2.2. Normalised values

Results presented in this study are normalised to facilitate comparison between different simulation cases and other similar studies with different turbines. The non-dimensional coefficients C_P and C_T are normalised via Eq. (8).

$$C_{Pnorm} = \frac{C_P}{C_{Pmax}} \tag{8}$$

In every simulation case, C_{Pmax} is the same value, which is the 0° Benchmark Case 1 value discussed in Section 3. The 0° Benchmark Case 1 C_P is normalised against itself to give a $C_{Pnorm} = 1$, and all other simulation results are normalised against the same C_{Pmax} value to highlight deviation from the 0° Benchmark Case 1 result.

2.3. Boundary conditions

All simulations use the same domain size and boundary conditions. The validation cases use a single turbine domain without a foundation in Section 3. The remaining simulation work uses the two-turbine multi-rotor foundation setup with the turbines in a downstream configuration, shown in Fig. 2. Here, both turbines are simulated with separate sliding mesh regions. Fig. 2 shows each face boundary condition definition and the distance from the device origin in turbine diameters (D). For the cases with flow misalignment, the foundation and turbines are rotated by the appropriate angle about the foundation's origin, as shown in Fig. 1.

A site-realistic velocity shear profile is defined at the domain inlet from Eq. (9). This is used from a study by Lewis et al. (2017) who deployed an Acoustic Doppler Current Profiler (ADCP) at the Morlais tidal site and measured values for the power law α, and the bed friction coefficient β, which can be used to determine a shear profile for a given hub-height free-stream velocity.

$$U_z = \left\{ \frac{z}{(\beta h)} \right\}^{\frac{1}{\alpha}} \bar{U} \tag{9}$$

2.4. Review of UK ADCP site data

Tidal sites are highly complex, and turbulence and changing flow misalignment are prevalent, Table 1. Tidal conditions are highly site-dependent, and inter-site variability can be extreme, with results depending on several factors, including location, deployment duration, and seasonal variation.

UK Government funding has been announced for projects at both the Morlais site in North Wales and the Pentland Firth Inner Sound site in Scotland (Department for Energy Security and Net Zero, 2026). Fixed yaw developers, such as HydroWing, have been awarded projects at the Morlais site, and as such, tidal ADCP data for the Morlais site is used as a case study, and a yaw misalignment angle of $\gamma = 16°$ is chosen as the maximum.

Applying an inflow angle of $\gamma = 16°$ to our model would assume that the tidal device is fully aligned with the incoming tide for one particular tidal cycle, and then experiences the largest yaw misalignment possible in the other. Although it is unrealistic for developers to deploy in this orientation, it does allow us to consider a worst-case scenario.

Where values for I or flood and ebb cycle asymmetry are not available in the referenced literature, the value "n/a" has been assigned in Table 1. In Table 1, I varies from 0.04 at the lower end, and 0.22 at the higher end, with the mean most commonly around 0.12–0.13, which we apply to our simulations as an initial condition. The turbulence intensity I can be calculated as a percentage using Eq. (10).

$$I = \frac{\sqrt{\bar{u'^2}}}{U} \tag{10}$$

2.5. Mesh independence

Meshing was conducted through the Star-CCM+ internal parts-based meshing tool, and mesh dependence was assessed using the Grid Convergence Index (GCI) method outlined by Celik et al. (2008). A coarse,

Table 1
ADCP data published in studies for tidal sites around the UK.

Location	I	Asymmetry	Data type	Authors
Morlais	n/a	0°–16°	ADCP Survey	Chisholm et al. (2025)
Ramsey Sound	0.12–0.18	0°	Turbine Deployment	Harrold and Ouro (2019)
Pentland Firth	0.10–0.13	30°	Turbine Deployment	Coles et al. (2018)
Fall of Warness	0.06–0.16	9°	Turbine Deployment	Parkinson and Collier (2016)
Sound of Islay	0.12–0.13	5°	ADCP Survey	Milne et al. (2013)
Strangford Lough	0.04–0.09	n/a	Turbine Deployment	MacEnri et al. (2013)

Table 2
Mesh refinement and GCI error with normalised critical variable values.

Mesh	Rotating domain	Stationary domain	Total	Critical variable	GCI
Coarse	2,265,872	3,420,501	7,952,245	0.9696	
Medium	5,151,247	8,072,786	18,375,280	1.0000	2.367%
Fine	12,897,426	19,589,003	45,383,855	1.0122	0.832%

medium, and fine mesh were simulated, and torque was used as the critical variable with values normalised by the medium mesh result. Each mesh cell count, and the GCI^{32}_{medium} and GCI^{21}_{fine} error are presented in Table 2. In Table 2, torque is normalised by the medium mesh value, and all values for mean torque are obtained by time-averaging the output over 3 steady revolutions. The medium mesh was chosen with a final cell count of 18,375,280, which includes the two rotating and stationary domains. For the Benchmark Case simulation models without a foundation frame, the same rotating domain mesh is used, with a total simulation cell count of 8,021,499.

The mesh employs unstructured polyhedral cells throughout the domain, except at the wall boundaries and region interfaces, where structured polyhedral cells are used to form inflation layers. The inflation layers are defined in terms of overall thickness, first layer cell height, and number of layers, to achieve a non-dimensional first layer height of $30 < y+ < 100$ along the blade's surface, and $y+ < 5$ along the foundation. The selection of $y+$ along the tower and turbine is driven by a requirement to maintain a $CFL < 1$ throughout the domain, and particularly at the turbine blade tips. The method for initially calculating these parameters to define the blade boundary layer inflation mesh is outlined by White (2006).

An internal Star-CCM+ feature, 'all $y+$ wall treatment', is applied, which switches between using blended wall functions for the mesh regions $30 < y+ < 100$, and resolves the boundary layer for mesh regions $y+ < 1$ (SIEMENS, 2023). Structured polyhedral cells are used at the interface between regions to obtain a conformal interface between the two subdomains at timestep $\Delta t = 0\ s$. As the mesh rotates, the structured cell faces at the interface become non-conformal, but have an alignment of over 99.99% as per Star-CCM+ guidelines. Between models, the same mesh refinement is used in rotating regions, with a different domain mesh used depending on the simulation case.

The commercial CFD solver Star-CCM+ was used for all simulations, and all model results reported are transient and feature a sliding mesh. The domain is initialised using results from a converged steady-state Moving Reference Frame (MRF) model on the same mesh, using a RANS $k - \omega$ SST turbulence model. The Δt timestep is set to $0.001\ s$ using implicit second-order unsteady time integration and is set to ensure a $CFL < 1$ along 98% of the blade. Each simulation is run for at least 10 revolutions, and results are taken for the final 3 steady turbine revolutions. A $0.1\ D$ length scale is applied as an initial condition. Turbulence intensity decay was observed in our models, a phenomenon which has also been observed in the literature, such as the works of Blackmore et al. (2014) and Badoe et al. (2024). A higher than default length scale was observed to reduce this I decay in our $k{-}\omega\ SST$ turbulence model, and as such has been applied. Table 3 displays the main CFD simulation parameters and initial boundary conditions.

The turbine blade is segmented into 21 equally spaced radial sections so that local torque and thrust values, and spanwise C_P and C_T coefficients can be calculated, similar to the method presented by Podeur et al. (2025). These sections are also used to locally refine the mesh along the blade length, shown in Fig. 3.

Table 3
CFD parameters and setup conditions.

Parameter	Value
Turbulence Model	$k - \omega$ SST
ΔT	$0.001s$
$y+_{tower}$	$y+ < 5$
$y+_{turbine}$	$30 < y+ < 100$
Wall treatment	All $y+$ wall functions
Inlet Velocity	2 m/s shear profile
Turbulence Intensity, I	0.12
Length Scale, l	0.1 D

2.6. Simulation cases

Table 4 displays the simulation cases to be run. Cases 1–4 are used in Section 3, for model validation and benchmarking. The impact of foundation shadowing and flow misalignment is then analysed by comparing four main simulation cases, Cases 5–8. The Shadowing CFD simulations use 2 different foundation variations, shown in Fig. 1. These are the No Fairing (NF) and the Extended Fairing (EF) variations. Cases 5 and 6 are the shadowing cases with the NF foundation for flow misalignment angles 0° and 16°. Cases 7 and 8 are the shadowing cases with the EF foundation model for the same flow misalignment angles. Each turbine is run at an optimal TSR, $\lambda_{opt} = 7$, which corresponds to the turbine's peak C_P efficiency. This operating condition is below rated power, but λ_{opt} provides a stable basis for evaluating the shadowing effect impact on turbine performance coefficients C_P and C_T.

2.7. Computational resource

Simulations were run on the Cirrus EPCC UK National Tier-2 HPC Service using 2x 36-core nodes and consumed approximately between 16,000 and 20,000 core-hours per simulation.

3. CFD benchmarking and validation

3.1. Aligned flow validation

Turbine CFD models with uniform flow velocity and low turbulence, referred to as Benchmark Cases 1–4, are run before the complexity of the foundation is added, and are used for model validation. These models have the same laterally spaced turbine configuration as in NF and EF Cases 5–8, but do not include the foundation frame.

The two available validation datasets used are a range of directly measured field samples from a full-scale Tocardo turbine test conducted by Tocardo at the European Marine Energy Centre (EMEC) in 2017, and a $1/6^{th}$ scale tank test campaign conducted by HydroWing. Neither dataset is published, but the normalised values are used here for CFD model validation.

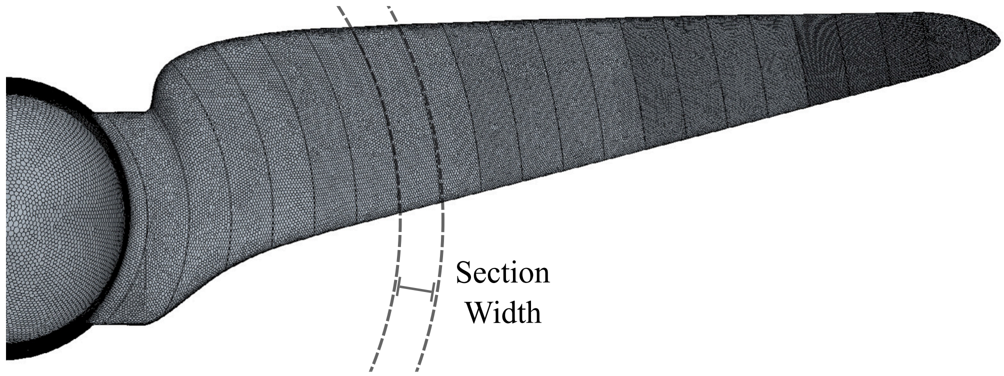

Fig. 3. Blade radial sections used for mesh refinement.

Table 4
Simulation case description.

Case	Simulation	Foundation included?	Misalignment angle, γ
Benchmark	1	No	0°
	2	No	8°
	3	No	16°
	4	No	24°
Shadowing NF	5	Yes	0°
	6	Yes	16°
Shadowing EF	7	Yes	0°
	8	Yes	16°

The Left plot of Fig. 4 displays the CFD results and the normalised tank experimental validation dataset. The experimental tests were conducted at a $1/6^{th}$ scale with a tank blockage ratio of $< 3\%$, a turbulence intensity of $< 5\%$, and a Reynolds number at 70% radius of $3e5$ calculated using Eq. (11).

$$Re_{0.7} = \frac{\rho U L_{0.7}}{\mu} \tag{11}$$

The tank testing values are reported for TSRs between 2.5 and 12 in 0.25 step increments. The CFD and experimental data show good correlation across the TSR range, with slight disparity in the underspeed TSR region.

The field data in the Right plot of Fig. 4 is scattered and noisy, but provides a foundation for validating the CFD model C_P vs TSR curve. The Benchmark CFD Case results are reported for TSR = 2, 4, 6, 7, 8, 10, 12, and show good agreement on both the peak TSR and the overspeed TSR range. Overall, the Benchmark CFD compares well to the available datasets, giving confidence in model results within the presented TSR range.

3.2. Yaw misalignment

C_P losses due to yaw misalignment, γ, can be initially estimated analytically using Eq. (12), which follows a $\cos^3$ curve (Jenkins et al., 2021).

$$C_P = C_P \cos^3(\gamma) \tag{12}$$

This analytical estimation does not account for factors such as $3D$ flow effects, blade shape, and turbine dimensions. To obtain a trend for our model of $C_{P_{norm}}$ against yaw misalignment, Benchmark Cases 2, 3, and 4 are simulated for misalignment angles of γ = 8°, 16°, and 24°. Fig. 5 compares our benchmark CFD results for yaw misalignment with analytical estimations and other published results from the literature. There is a large variety between studies, with our benchmark results tending towards the $\cos^2$ curve, along with experimental results from Bahaj et al. (2007) and O'Rourke et al. (2015). Results from Galloway et al. (2011) are between both curves, with results from Frost et al. (2017) tending more towards the $\cos^3$ curve.

Specific flow physics and experimental or modelled Reynolds numbers will influence results, making it hard to draw comparisons between results. However, the general trends suggest that the power generated by a turbine in yaw will usually outperform the $\cos^2$ and $\cos^3$ curves often used for analytical estimation. The Benchmark Case results for the yawed γ = 8°, 16°, and 24° simulations are ≈2.2%, ≈7%, and ≈14%, respectively.

The time-dependent C_P results for Benchmark Case 3 at 16° misalignment are presented in the Right plot of Fig. 7. Here, the C_P oscillates through the revolution as the most forward-facing turbine blade is more highly loaded than the rear blade. Combined with the velocity shear profile present in the domain, this causes a slight oscillation of torque and thrust. The C_P peaks when the forward blade is highest in the water column, and troughs when the forward blade is lower in the water column. Benchmark Cases 2, 3, and 4 are used to quantify the expected loss purely due to flow misalignment and compare against 16° NF Case 6 and EF Case 8 to determine shadowing losses.

4. Results

4.1. Shadowing effects for the No fairing models

Tip vortices are shed from the two-bladed HATT before blending into the larger turbine wake downstream. Additional vortices from the foundation structure are shed in sheets and travel downstream, where they collide with the turbine blades, seen in Fig. 6. As the wake is effectively a region of ambient velocity deficit, loading on the blades decreases as they pass through the shadow, inducing a blade pulsating force.

Fig. 7 shows fluctuations in time-dependent $C_{P_{norm}}$ as the blades pass through the foundation wake shadow for the final 3 revolutions of 0° and 16° Benchmark Cases 1 and 3, and NF and EF Cases 5–8. For each case, there is a trend for two larger and two smaller fluctuations per revolution. The turbine blades are vertical at blade phase angles,

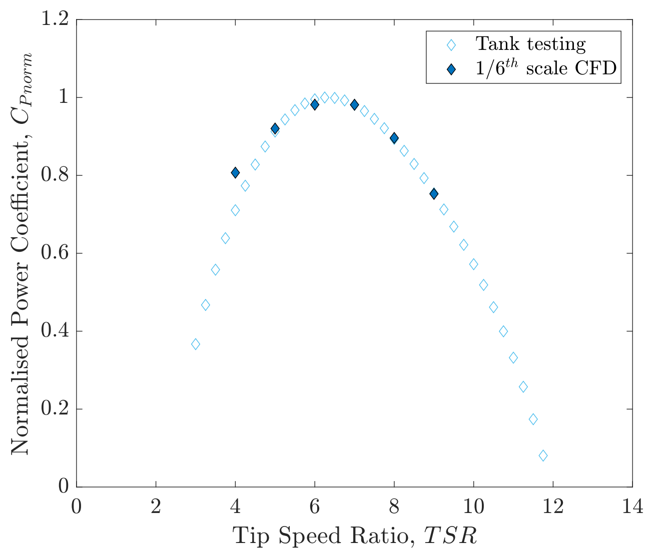

(a)

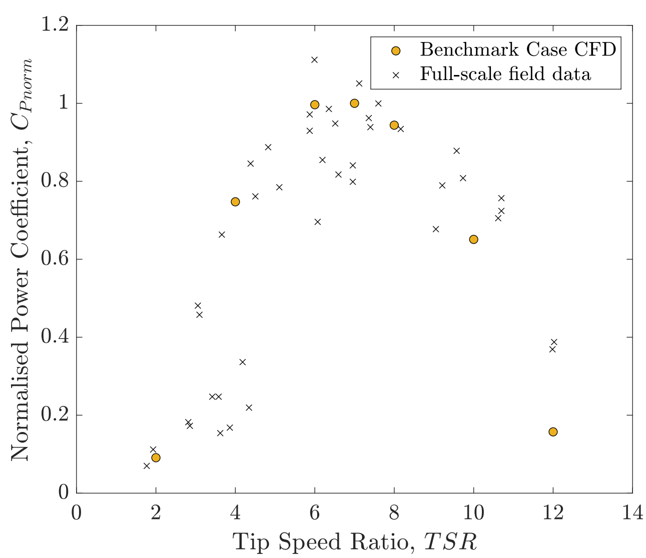

(b)

Fig. 4. Benchmark CFD C_P results validation. (a) $1/6^{th}$ Scaled CFD model and tank testing. (b) Full-scale CFD model and field data.

$\theta = 0°$ and 180° and are horizontal at $\theta = 90°$ and 270°. The larger C_P fluctuations occur as the blades are near vertical and directly behind the foundation in its shadow, with the smaller two fluctuations caused by the horizontal wing shadow.

Comparing Figs. 7 and 8, we see that C_T loading is less impacted by the shadowing effect than C_P. We know from Eqs. (6) and (7) that C_P is proportional to U^3 and C_T loading to U^2, and thus the velocity deficit from the foundation shadowing wake has a more significant impact on C_P when comparing performance coefficients.

4.1.1. 0° No fairing case 5

Fig. 6 shows the foundation shadow isosurface wake for the 0° NF Case 5 model. As the turbine blades pass vertical, the bottom blade enters the velocity deficit wake, decreasing loading. From this, the 0° NF Case 5 turbine C_{Pnorm} in Fig. 7 drops by ≈ 25–30%. Overall, along with the two smaller fluctuations at blade phase angles, θ, of 90° and 270°, this results in a ≈ 4.6% reduction in mean C_{Pnorm} against the free stream 0° Benchmark Case 1 results.

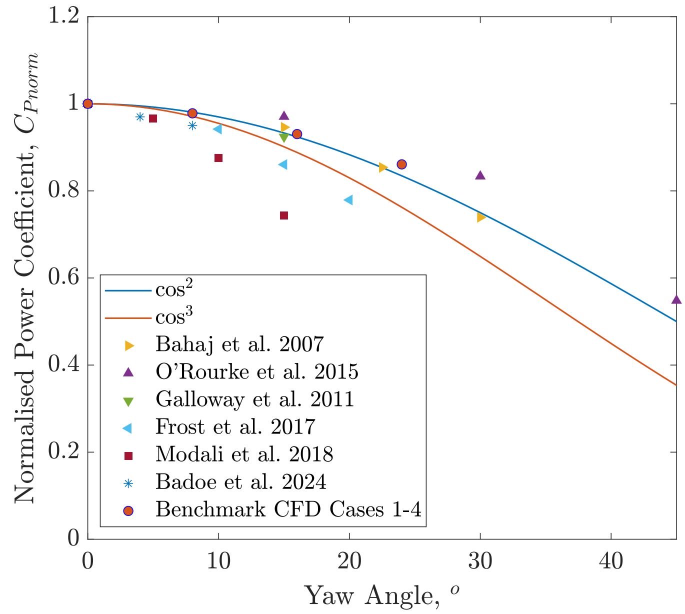

Fig. 5. Published data on yaw misalignment compared to cases from literature (Bahaj et al., 2007; O'Rourke et al., 2015; Galloway et al., 2011; Frost et al., 2017; Modali et al., 2018; Badoe et al., 2024).

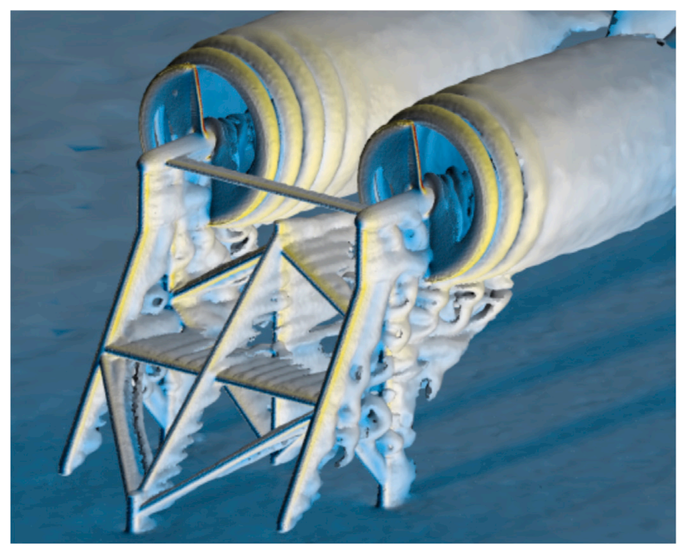

Fig. 6. Isosurface vortices for the 0° NF Case 5 model.

The turbine C_T loading for 0° Benchmark Case 1 and the Shadowing Cases 5–8 are compared in Fig. 8. Turbine C_T drops at the blades' vertical position similarly to C_P. Through the following 30°, this returns to the free-stream thrust values with smaller fluctuations induced by the horizontal wing.

4.1.2. 16° No fairing case 6

The yaw misalignment impact on the shadowing severity is observed by comparing the C_{Pnorm} results for the 0° and 16° cases in Fig. 7. At higher misalignment angles, the foundation has a greater projected area, which increases its wake width. The turbine blades now spend a longer proportion of the revolution in the foundation shadow.

We can observe this effect in Fig. 9 by comparing the Top Left and Top Right figures. Here, a plane at $z = 17m$ displays a velocity contour for each Case. Not only does the turbine at $\gamma = 16°$ yaw misalignment now have a reduced effective swept area, but the foundation shadow

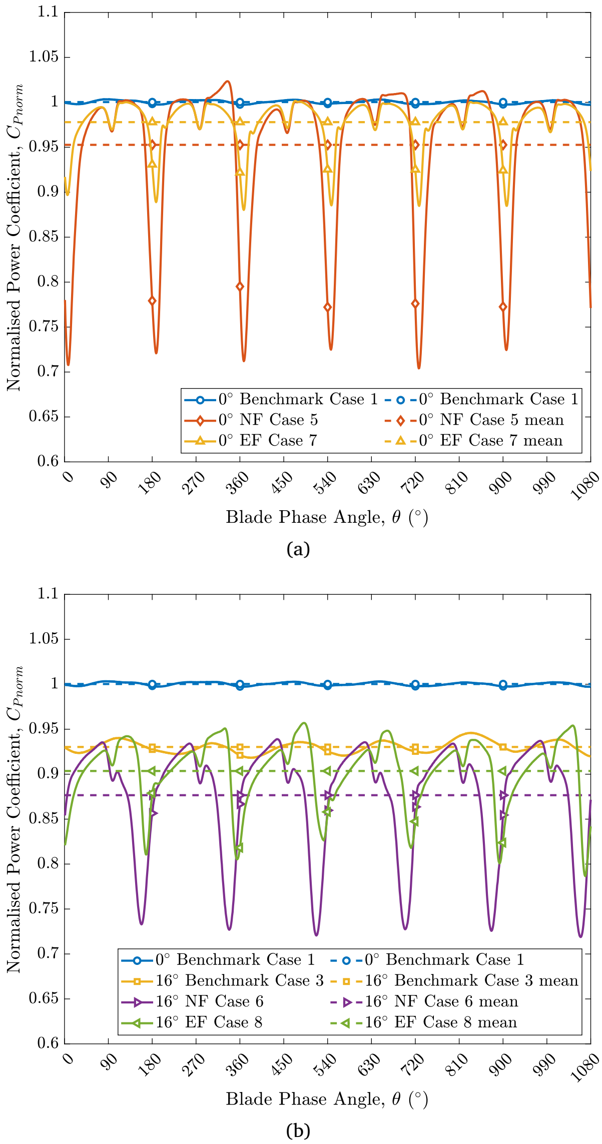

Fig. 7. Plot showing the time-dependent and mean $C_{P_{norm}}$ values over 3 steady revolutions. (a) 0° Aligned flow Cases 5 and 7. (b) 16° Misaligned flow Cases 6 and 8. Line markers are placed every θ = 180°, indicating that the turbine blades are vertical.

is wider and covers a larger proportion of that swept area. This effect is evident by comparing the largest fluctuations between cases 0° NF Case 5 and 16° NF Case 6 in Fig. 7, where the 16° NF Case 6 $C_{P_{norm}}$ is reduced for more of the turbine phase angle.

From Section 3.2, an isolated turbine will experience a ≈7% drop in mean $C_{P_{norm}}$ at γ = 16° due to yaw misalignment alone. In total, the mean $C_{P_{norm}}$ for 16° NF Case 6 drops by ≈12.4% against the free stream 0° Benchmark Case 1. Attributing ≈ 7% of this to yaw misalignment suggests that ≈ 5.4% is caused by foundation shadowing.

This is assuming that an isolated turbine in a 16° yawed inflow behaves equally to the turbine in 16° NF Case 6 when the foundation is included. When the foundation shadowing effect is coupled with a yawed inflow, there is increased uncertainty in the results, and we cannot say with confidence that the behaviour is the same. For this study, we are assuming that both turbines experience a ≈ 7% loss from the yawed inflow angle regardless of whether the foundation is included in the model or not.

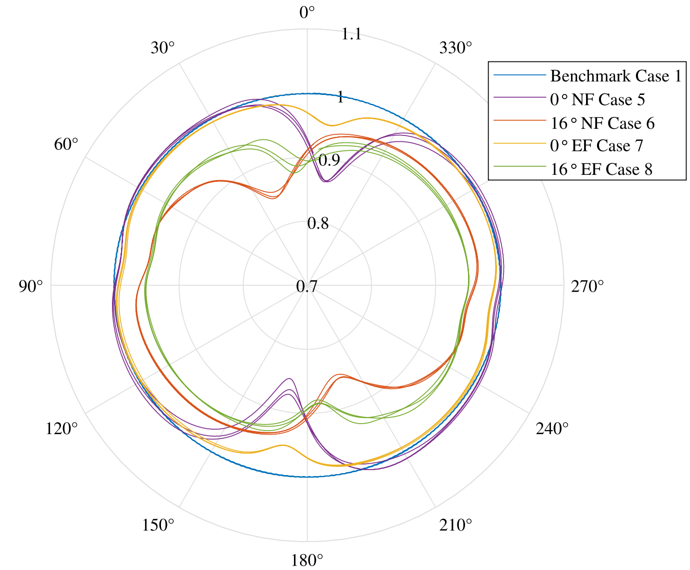

Fig. 8. Normalised C_T polar plot over 3 revolutions.

This effect is increased compared to 0° NF Case 5, where shadowing losses are ≈ 4.6%, suggesting that the shadowing mean $C_{P_{norm}}$ losses are approximately 1% worse at higher yaw misalignment angles.

4.2. Shadowing effects for the extended fairings model

4.2.1. 0° extended fairing case 7

The fluctuations in time-dependent C_P for 0° EF Case 7 from Fig. 7 are significantly reduced as compared to 0° NF Case 5, thanks to the fairing. Reduced foundation flow separation results in a smaller wake and a smoother turbine torque output. The pulses in time-dependent C_P for 0° EF Case 7 are now ≈ 10%, down from ≈ 25–30% for 0° NF Case 5, and the loss in mean $C_{P_{norm}}$ is now only ≈2.2% over a revolution, compared to ≈ 4.6% without fairings. As expected, with no change in design, the horizontal wing beam shadowing fluctuations are similar for all models.

4.2.2. 16° extended fairing case 8

The symmetrical fairings are equally effective at mitigating C_P losses at higher flow misalignment angles. Flow separation is reduced, and so is the shadow wake width, which reduces fluctuations along the blades.

The 16° EF Case 8 has a mean $C_{P_{norm}}$ of ≈ 9.7%, which, when accounting for the ≈ 7% yaw misalignment, means that approximately ≈ 2.7% can be attributed to the shadowing effect using an additive assumption. Comparing this result to the 0° EF Case 7 mean $C_{P_{norm}}$ of ≈ 2.2% again suggests that the shadowing effect becomes more severe at higher yaw misalignment angles. However, at γ = 16°, the most significant losses come from the ≈ 7% $C_{P_{norm}}$ yaw misalignment losses rather than the foundation shadowing effect.

4.3. Rotor plane distributed power coefficient

We now analyse the data for the C_P distribution for a single blade over the whole rotor plane to understand in more detail the foundation shadow effect on turbine performance. To obtain this data, the blade profile is split into 21 radial sections, seen in Fig. 3, where C_T and C_P are recorded for each section, following a similar method as presented in Podeur et al. (2025).

Fig. 10 displays the normalised C_P distribution across blade length for the Benchmark Cases 1 and 3 in undisturbed flow at 0° and 16°

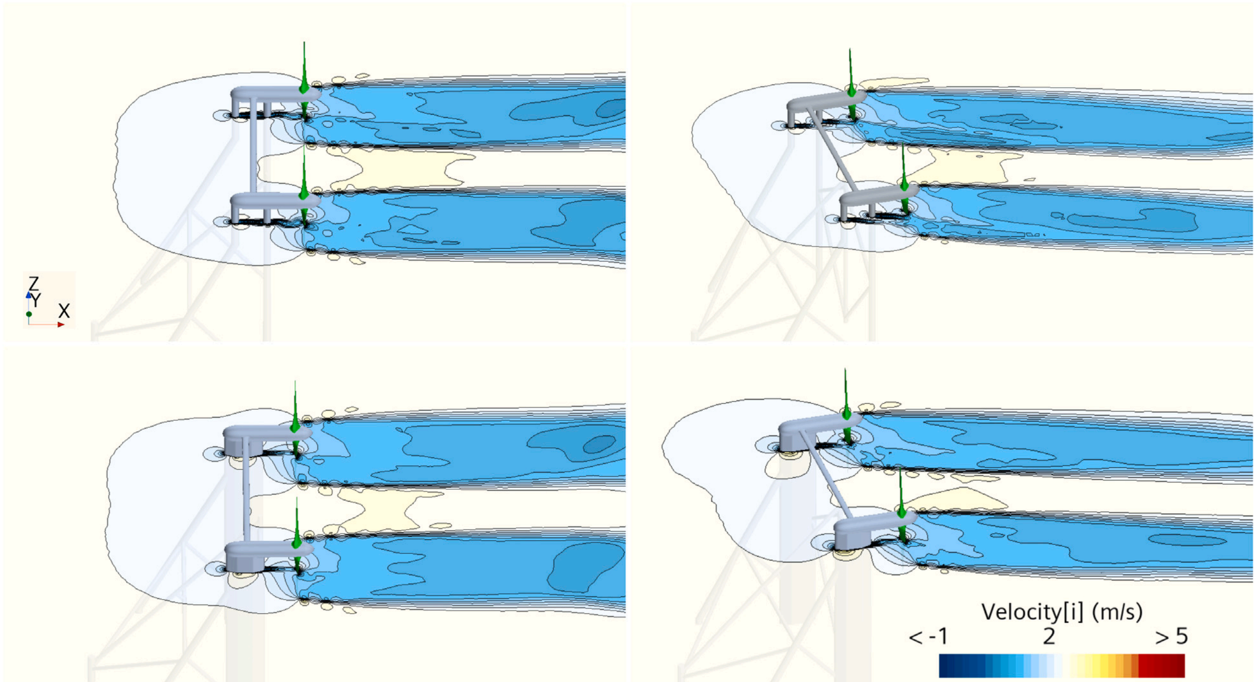

Fig. 9. Velocity contours in the positive x-axis for the range $-1 < velocity(i) < 5$ along a plane at $z = 17$ m. (Top Left) 0° NF Case 5. (Top Right) 16° NF Case 6. (Bottom Left) 0° EF Case 7. (Bottom Right) 16° EF Case 8.

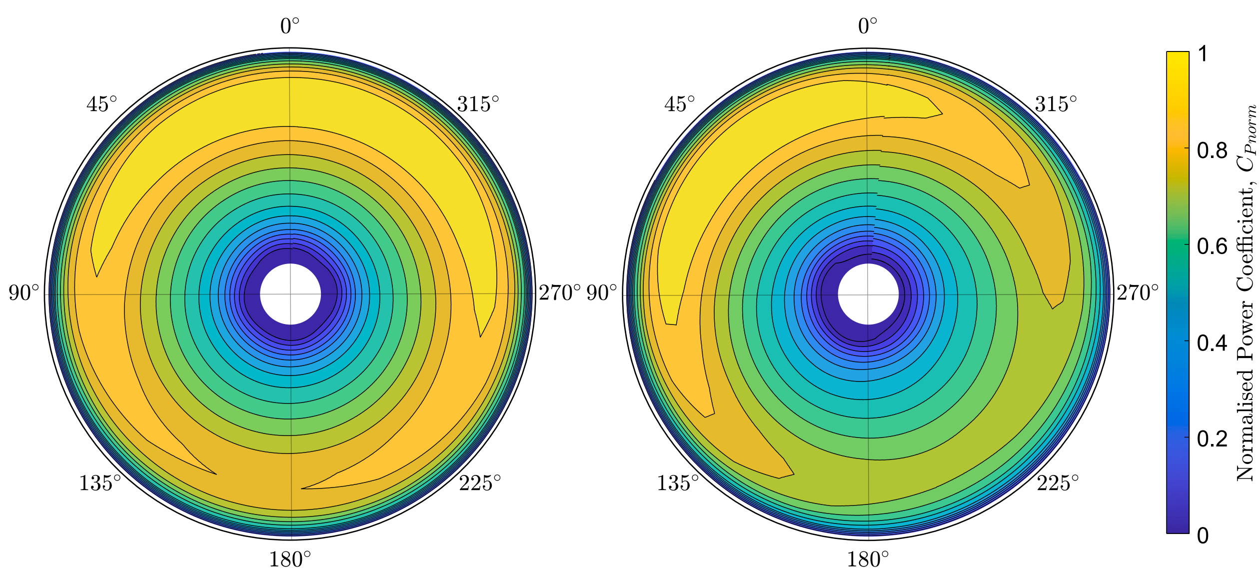

Fig. 10. Distributed blade normalised C_P for 0° and 16° Benchmark Cases 1 and 3 for a single blade.

yaw misalignment. The highest C_P is in the final $1/3^{rd}$ blade length, decreasing towards the blade root. Velocity shear profile effects are visible here, as C_P increases higher up in the water column.

Fig. 11 shows the normalised C_P distribution for Cases 5–8. The darker region at $\theta \approx 180°$ corresponds to the largest fluctuation in C_P previously shown in Fig. 7. The horizontal wing beam impact is visible at $\theta \approx 90°$, although less severe than the vertical beam's response at $\theta \approx 180°$ due to the reduced wing profile, which helps mitigate shadowing severity. For the remainder of the revolution, between $\theta =$ 90°–180°, the turbine blade generates mostly free stream values for C_P in unobstructed flow, Fig. 10.

There is a noticeable difference in distributed C_P when comparing the 0° and 16° cases, primarily in the location of maximum deficit, which has shifted 10° ∼ 20° anti-clockwise due to the enlarged foundation wake width at higher flow misalignment angles. Because of this, the blade spends a longer proportion of its revolution in the foundation shadow, increasing the region of C_P deficit and further reducing $C_{P_{mean}}$. Comparing the NF and EF cases in Fig. 11, there is a visible reduction in wake width with the EF cases for aligned and misaligned flow.

5. Discussion

5.1. On foundation shadowing for aligned flow

When the turbines and foundation, with 0.06 D tower diameters, are aligned with the incoming flow, our results show that shadowing

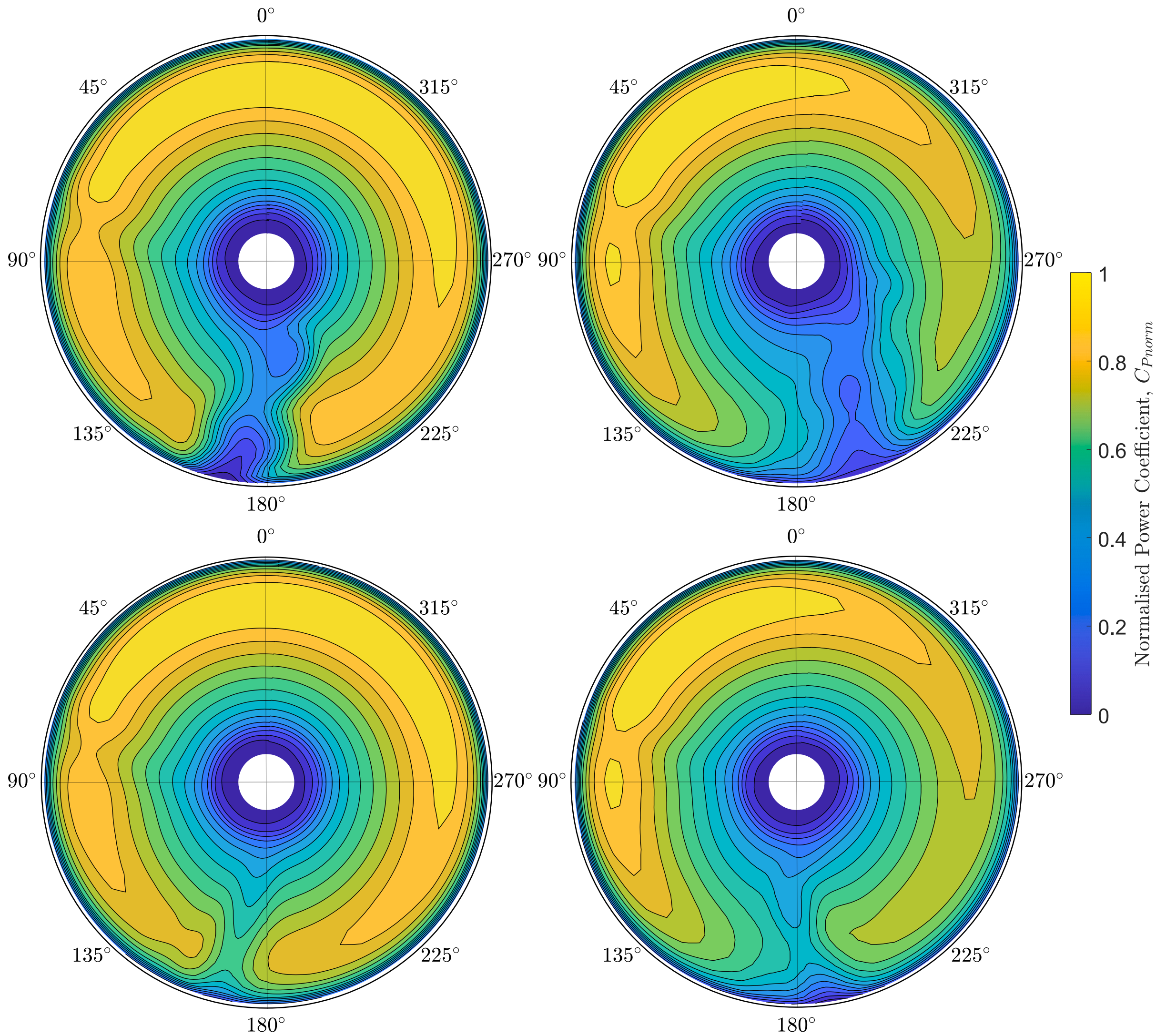

Fig. 11. Distributed blade normalised C_P for a single blade. (Top Left) 0° NF Case 5. (Top Right) 16° NF Case 6. (Bottom Left) 0° EF Case 7. (Bottom Right) 16° EF Case 8.

losses of ≈ 4.6% in mean C_{Pnorm} can be expected. This loss occurs as the blade loading reduces whilst it passes directly behind the foundation and through its wake, formed by flow separation and vortex shedding in Figs. 6 and 9.

Sections 4.1 and 4.2 describe the foundation's impact on turbine mean C_P and C_T, which is clearly linked to two main factors. The D_t/D ratio and the foundation tower shape. Once a fairing is included, similar to the horizontal 2:1 oval wing beam, and mean C_{Pnorm} losses are reduced to ≈ 2.2%.

Frost et al. (2015) studied the effect of increasing the clearance distance between the tower and rotor on the foundation shadow effect. They simulated a reduction in mean C_{Pnorm} of between 6–9% depending on clearance distance for a monopile foundation with a 0.24 D tower diameter (D_t/D) and three-bladed turbine. A key deviation between the present study and the work by Frost et al. (2015) is the difference between a two-bladed and a three-bladed turbine. A two-bladed turbine will experience fewer fluctuations per revolution, but as each blade makes up a larger proportion of the mean, each load fluctuation will have a greater impact on the mean. Additionally, the load imbalance across the two blades is maximised when in the vertical position, as the upper blade experiences the higher flow velocities in the water column, and the lower blade thrust loading is reduced in the foundation shadow wake. Conversely, a three-bladed turbine can better balance the torque output and will experience less loading imbalance between blades.

A simple multi-rotor support foundation was simulated for aligned flow, in the preliminary work to this study (Townley et al., 2025). In that study, the multi rotor foundation had an effective 0.2 D tower diameter, made up of two 0.1 D cylindrical beams in the horizontal and vertical directions. Losses in mean C_{Pnorm} were approximately ≈ 10% over a revolution due to shadowing.

Considering the results in this presented study, and in the works of Frost et al. (2015), Guo et al. (2020), and Townley et al. (2025), the general trend continues in that by decreasing the foundation tower D_t/D ratio, we can reduce the foundation shadow effect on mean C_P and C_T. This confirms that reducing the diameter of structural components immediately upstream of the turbine by designing with D_t/D ratios in mind is the most effective method of reducing the foundation shadow effect severity.

5.1.1. Foundation fairing

Mason-Jones et al. (2013) demonstrated that for a turbine upstream of its support tower, an elliptical monopile had lower thrust loading acting on the tower and was more hydrodynamic than circular or diamond-shaped support towers. We have applied these findings to a fixed-yaw downstream turbine impacted by the foundation shadow effect, and demonstrated that efficiency losses can be significantly reduced through relatively simple design changes, as seen in Fig. 7.

Fig. 9 shows that the fairing effectively reduces downstream foundation wake width and the impact on turbine performance coefficients. The benefit of this is seen in Fig. 11, which shows the azimuthal distribution of C_{Pnorm}. Figs. 10 and 11 show 'hotspot' areas where C_{Pnorm} is high, and where it is lowered by the foundation shadow effect. The fairing's effectiveness is demonstrated by comparing the 0° NF Case 5 and 0° EF Case 7 results in Fig. 11. A turbine blade in the free stream has the highest C_P at $0.7-0.9$ r/R. The 0° NF Case 5 C_{Pnorm} has reduced by ≈ 0.75 for the r/R 0.7–0.9 blade section at $\theta = 180°$, whereas 0° EF Case 7 C_{Pnorm} has reduced by ≈ 35% in the same location.

These results demonstrate that for a tidal foundation with tower diameters of ≈ 0.06 D, fairings can be an effective solution for reducing the mean C_{Pnorm} foundation shadow effect losses from ≈ 4.6% to within ≈ 2.2% in rectilinear tides. For tidal developers deploying at sites aligned in the flood and ebb cycles, using fairings on a multi-rotor device with smaller D_t/D ratios could be an alternative to using an active yaw system when expecting to operate at the site for 20–25+ years.

5.2. On foundation shadowing for misaligned flow

The effect of flow misalignment is significant. The foundation's frontal exposed area is increased at $\gamma = 16°$, and sections which were faired to reduce wake width at $\gamma = 0°$ are now out of plane. The turbine spends a longer proportion of its revolution in the foundation shadow, increasing the magnitude of fluctuations in C_P and C_T.

Comparing the 16° NF Case 6 and EF Case 8 results in the top and bottom right plots of Fig. 11, we see that between $\theta = 180° < \theta < 225°$ the faired model retains a higher C_P. The dark blue region in the 16° NF Case 6 plot shows a significant reduction in C_{Pnorm} for the 0.7–0.9 r/R blade section. This is much improved once the fairing is included, and the turbine can retain a higher efficiency as the foundation wake is streamlined.

Although the foundation shadow effect is marginally worse at higher misalignment angles, the most significant reduction to C_P comes from the turbine yaw losses themselves. In Fig. 5, published turbine performance data under yaw misalignment from the literature is compared to show that C_{Pnorm} typically follows a $\cos^{\alpha}$ curve for α values between 2–3. In our case, the two-bladed turbine follows a $\cos^2$ curve, with C_{Pnorm} losses of ≈ 7% at $\gamma = 16°$. Considering the literature cases, C_{Pnorm} losses at $\gamma = 15°$ may range from ≈ 3%–16%. Assuming the more conservative estimates, the yaw losses are more significant than shadowing at higher misalignment angles.

Misalignment data for UK tidal sites displayed in Table 1 shows that the typical flood and ebb cycle asymmetry is highly site dependent. By considering this study's findings during the array layout phase, tidal developers at rectilinear flow sites may avoid active components by utilising fixed yaw bidirectional turbines to improve reliability.

At sites with higher misalignment, developers must contend with both losses due to reduced turbine swept area and the shadowing effect. For the non-faired cylindrical tower sections, 0° and 16° NF Cases 5 and 6, the forces normal to the flow fluctuate ± about zero, and the drag forces dominate. This is also true for the aligned flow extended fairing model, 0° EF Case 7, as the bidirectional fairing does not generate a pressure difference for $\gamma = 0°$. However, for 16° EF Case 8, the angle of attack between the tower fairing and the free stream flow creates a sustained force on the structure normal to the flow and the lift to drag ratio, or normal to streamwise force ratio, is around 4.5. Although tower fairings have been shown to reduce flow separation, their use at sites with high flood and ebb misalignment might not be viable due to increased structural loading at misalignment angles $\gamma \neq 0°$. The symmetrical fairing can operate effectively without increasing structural loads when assuming aligned flow, but flow misalignment will increase loading in the cross-stream direction.

5.3. Turbine power azimuthal variation

Having applied a velocity shear profile to the model in Eq. (9), we would expect each blade to generate maximum torque when vertical at the highest point in its azimuth, and then generate minimum torque at its lowest point when vertically downward. However, considering the 0° Benchmark Case 1 in Fig. 10, this is not strictly the case. The max C_{Pnorm} lags the 0° azimuth peak by ≈ 20°, and the same is true for the minimum C_{Pnorm}, which occurs closer to 200°. This lag is likely a consequence of rotational wake and induction region interactions, and this phenomenon has also been noted in other studies.

Mason-Jones et al. (2013) with their CFD model of a three-bladed tidal turbine, surmised that this was due to an interaction between the turbine blades and the downstream wake influencing the upstream velocity shear. Ahmed et al. (2017) used an LES model to simulate a 1 MW tidal turbine, and also observed a similar lag in the maximum power generation point. They concluded that the point of turbine maximum power was a function of turbine phase angle, dependent on the velocity shear profile, I, length scale, tower passing frequency, and other model boundary conditions. Considering our 16° Benchmark Case 3 model in Fig. 10, we see again that the point of maximum and minimum C_{Pnorm} has shifted from the expected $\theta = 0°$ and 180° phase angle locations. Here, the combination of factors mentioned above from studies by Mason-Jones et al. (2013) and Ahmed et al. (2017) as well as the $\gamma = 16°$ yaw misalignment means that the upstream blade is most highly loaded, resulting in an asymmetrical C_{Pnorm} polar plot in Fig. 10.

5.4. Study limitations

Here, we acknowledge methodology limitations that have impacted this study. As the primary focus was the dynamic interaction between turbine and structure, it was deemed necessary to simulate the setup with a transient CFD model rather than use a lower fidelity alternative. Although the RANS $k-\omega$ SST model effectively captured some vortex-shedding dynamics from the foundation, unlike higher-fidelity models such as LES, the RANS model cannot resolve fine turbulent eddies or inflow turbulence that would be present at the site.

Although tower fairings have been shown to reduce flow separation, these may only be viable at rectilinear sites when considering perfect alignment between the turbine rotational axis and incoming flow because of increased structural loading at $\gamma \neq 0°$ for fairings compared to cylindrical cross-sections. Here, we have presented multiple cases considering the shadowing effects on turbine performance and loading. The effects of structural loading, particularly at flow alignment angles $\gamma \neq 0°$, are considered in future work.

In our analysis of foundation losses in a yawed inflow, we have assumed that the turbine behaviour in yaw is the same and that C_P losses are ≈ 7% for $\gamma = 16°$ for both the isolated turbine and for the turbine+foundation model. This assumption enables us to attribute some percentage of the overall C_P losses for the 16° NF and EF Cases 6 and 8 directly to the foundation shadowing effect.

Another limitation is the number of operating conditions considered. This study considers a single current flow velocity and TSR for two misalignment angles. Future work should consider additional complexity from wave current interactions or a greater range of operating conditions. Waves coming from a perpendicular angle could temporarily increase the resultant incoming flow angle above 16°, causing the vertical fairing to "stall" and introducing a further complexity into the analysis as flow separation increases.

6. Conclusion

This study investigates foundation shadowing and yaw misalignment effects on a fixed-yaw turbine operation downstream of its multi-rotor foundation, with reduced D_t/D tower diameters. A case study foundation and turbine were used from the industry, and the CFD model was validated against physical datasets from field data and tank test experiments.

The primary study results showed that:

- The foundation shadow effect causes fluctuations in C_P and C_T loading as the blades pass through the tower wake, significantly affecting turbine performance. The most effective solution for mitigating the shadowing effect is to reduce the tower D_t/D ratios, regardless of cross-sectional shape.
- For rectilinear flow, tower fairings can reduce flow separation and load fluctuations along the blades to further improve turbine C_P performance when shadowed.
- Higher flow misalignment angles increase the foundation's exposed frontal area and move the turbine's rotational axis out of plane with the flow. Here, turbine yaw losses become more significant than shadowing losses as the misalignment angle increases.
- Tower fairings at high yaw misalignment angles can reduce a proportion of the shadowing effect severity as shown, but are ineffective against turbine yaw misalignment losses, and increased structural loading normal to the flow direction in this configuration may prove sub-optimal.
- For rectilinear tidal sites, bidirectional turbines with a low tower to turbine diameter D_t/D ratio may be considered as an alternative to active yaw systems to mitigate the foundation shadow effect.

CRediT authorship contribution statement

Bryn Townley: Writing – original draft, Visualization, Validation, Formal analysis, Conceptualisation. **Qing Xiao:** Writing – review & editing, Supervision, Formal analysis. **Athanasios Angeloudis:** Writing – review & editing, Supervision, Formal analysis. **Ian Ashton:** Writing – review & editing, Supervision, Formal analysis. **George Dadd:** Writing – review & editing, Supervision, Formal analysis.

Declaration of competing interest

The authors declare the following financial interests/personal relationships which may be considered as potential competing interests: Bryn Townley reports financial support was provided by Engineering and Physical Sciences Research Council. Bryn Townley reports financial support was provided by UK Research and Innovation Natural Environment Research Council. Bryn Townley's IDCORE Engineering Doctorate is sponsored by HydroWing. If there are other authors, they declare that they have no known competing financial interests or personal relationships that could have appeared to influence the work reported in this paper.

Acknowledgements

B. Townley thanks the EPSRC and NERC for project funding through the IDCORE programme, and HydroWing for project data and technical support. This work was completed as part of the Industrial Centre for Doctoral Training for Offshore Renewable Energy (IDCORE) funded by the EPSRC and NERC (EP/S023933/1). This work used the Cirrus UK National Tier-2 HPC Service at EPCC (http://www.cirrus.ac.uk) funded by the University of Edinburgh and EPSRC (EP/P020267/1).

References

Ahmed, U., Apsley, D.D., Afgan, I., Stallard, T., Stansby, P.K., 2017. Fluctuating loads on a tidal turbine due to velocity shear and turbulence: Comparison of CFD with field data. Renew. Energy 112, 235–246. http://dx.doi.org/10.1016/j.renene.2017.05.048.

Badoe, C.E., Li, X., Williams, A.J., Masters, I., 2024. Output of a tidal farm in yawed flow and varying turbulence using GAD-CFD. Ocean Eng. 294 (January), 116736. http://dx.doi.org/10.1016/j.oceaneng.2024.116736.

Bahaj, A.S., Molland, A.F., Chaplin, J.R., Batten, W.M., 2007. Power and thrust measurements of marine current turbines under various hydrodynamic flow conditions in a cavitation tunnel and a towing tank. Renew. Energy 32 (3), 407–426. http://dx.doi.org/10.1016/j.renene.2006.01.012.

Blackmore, T., Batten, W.M., Bahaj, A.S., 2014. Influence of turbulence on the wake of a marine current turbine simulator. Proc. R. Soc. A: Math. Phys. Eng. Sci. 470 (2170), http://dx.doi.org/10.1098/rspa.2014.0331.

Celik, I.B., Ghia, U., Roache, P.J., Freitas, C.J., Coleman, H., Raad, P.E., 2008. Procedure for estimation and reporting of uncertainty due to discretization in CFD applications. J. Fluids Eng. Trans. the ASME 130 (7), 0780011–0780014. http://dx.doi.org/10.1115/1.2960953.

Chisholm, J.E., Roberts, M., Powell, B., Rowlands, S., Robins, P., Roome, E., Hughes, P., Owen, A., Milford, C., Amjadian, P., Neill, S.P., 2025. Resource characterization of a commercial tidal stream energy site: Morlais, Irish Sea. Renew. Energy 247 (March), http://dx.doi.org/10.1016/j.renene.2025.122952.

Coles, D., Greenwood, C., Vogler, A., Walsh, T., Taaffe, D., 2018. Assessment of the turbulent flow upstream of the Meygen Phase 1A tidal stream turbines. Awtec2018.

Department for Energy Security and Net Zero, 2026. Contracts for Difference Allocation Round 7a Results. Technical Report, UK Government, URL https://www.gov.uk/government/publications/contracts-for-difference-cfd-allocation-round-7-results.

Dose, B., Rahimi, H., Stoevesandt, B., Peinke, J., 2020. Fluid-structure coupled investigations of the NREL 5MW wind turbine for two downwind configurations. Renew. Energy 146, 1113–1123. http://dx.doi.org/10.1016/j.renene.2019.06.110.

Finnegan, W., Fagan, E., Flanagan, T., Doyle, A., Goggins, J., 2020. Operational fatigue loading on tidal turbine blades using computational fluid dynamics. Renewable Energy 152, 430–440. http://dx.doi.org/10.1016/j.renene.2019.12.154.

Frost, C.H., Evans, P.S., Harrold, M.J., Mason-Jones, A., O'Doherty, T., O'Doherty, D.M., 2017. The impact of axial flow misalignment on a tidal turbine. Renew. Energy 113, 1333–1344. http://dx.doi.org/10.1016/j.renene.2017.07.006.

Frost, C., Morris, C.E., Mason-Jones, A., O'Doherty, D.M., O'Doherty, T., 2015. The effect of tidal flow directionality on tidal turbine performance characteristics. Renew. Energy 78, 609–620. http://dx.doi.org/10.1016/j.renene.2015.01.053.

Galloway, P.W., Myers, L.E., Bahaj, A.S., 2011. Experimental and Numerical Results of Rotor Power and Thrust of a Tidal Turbine Operating at Yaw and in Waves. Proc. the World Renew. Energy Congr. 57, 2246–2253. http://dx.doi.org/10.3384/ecp110572246.

Guo, B., Wang, D., Zhou, X., Shi, W., Jing, F., 2020. Performance evaluation of a tidal current turbine with bidirectional symmetrical foils. Water (Switzerland) 12 (1), http://dx.doi.org/10.3390/w12010022.

Harrold, M., Ouro, P., 2019. Rotor Loading Characteristics of a Full-Scale Tidal Turbine. Energies 1–19. http://dx.doi.org/10.3390/en12061035.

Jenkins, N., Burton, T., Bossanyi, E., Sharpe, D., Graham, M., 2021. Wind Energy Handbook, third ed. John Wiley and Sons Ltd, http://dx.doi.org/10.1002/9781119451143.

Jonkman, J., Butterfield, S., Musial, W., Scott, G., 2009. Definition of a 5-MW reference wind turbine for offshore system development. NREL Tech. Rep. (February), 1–75.

Larwood, S.M., Chow, R., 2016. Comparison of upwind and downwind operation of the NREL Phase VI Experiment. J. Phys.: Conf. Ser. 753 (2), http://dx.doi.org/10.1088/1742-6596/753/2/022041.

Lewis, M., Neill, S.P., Robins, P., Hashemi, M.R., Ward, S., 2017. Characteristics of the velocity profile at tidal-stream energy sites. Renew. Energy 114, 258–272. http://dx.doi.org/10.1016/j.renene.2017.03.096.

MacEnri, J., Reed, M., Thiringer, T., 2013. Influence of tidal parameters on SeaGen flicker performance. Philos. Trans. R. Soc. A: Math. Phys. Eng. Sci. 371 (1985), http://dx.doi.org/10.1098/rsta.2012.0247.

Mason-Jones, A., O'Doherty, D.M., Morris, C.E., O'Doherty, T., 2013. Influence of a velocity profile & support structure on tidal stream turbine performance. Renew. Energy 52, 23–30. http://dx.doi.org/10.1016/j.renene.2012.10.022.

Milne, I.A., Sharma, R.N., Flay, R.G., Bickerton, S., 2013. Characteristics of the turbulence in the flow at a tidal stream power site. Philos. Trans. R. Soc. A: Math. Phys. Eng. Sci. 371 (1985), http://dx.doi.org/10.1098/rsta.2012.0196.

Modali, P.K., Kolekar, N.S., Banerjee, A., 2018. Performance and wake characteristics of a tidal turbine under yaw. In: International Marine Energy Journal, vol. 1, (1), pp. 41–50. http://dx.doi.org/10.36688/imej.1.41-50.

Muchala, S., Willden, R., 2018. Influence of support structures on tidal turbine power output. J. Fluids Struct. 83, 27–39. http://dx.doi.org/10.1016/j.jfluidstructs.2018.08.008.

O'Rourke, F., Boyle, F., Reynolds, A., Kennedy, D.M., 2015. Hydrodynamic performance prediction of a tidal current turbine operating in non-uniform inflow conditions. Energy 93, 2483–2496. http://dx.doi.org/10.1016/j.energy.2015.10.078.

Parkinson, S.G., Collier, W.J., 2016. Model validation of hydrodynamic loads and performance of a full-scale tidal turbine using Tidal Bladed. Int. J. Mar. Energy 16, 279–297. http://dx.doi.org/10.1016/j.ijome.2016.08.001.

Podeur, V., Michaud, L., Groulx, D., Jochum, C., 2025. Downstream tidal turbine transient local blade loading characterization. Ocean Eng. 332 (July 2024), http://dx.doi.org/10.1016/j.oceaneng.2025.121419.

SIEMENS, 2023. Simcenter Star-CCM+ 2310 User Guide.

Smith, R., Townley, B., Wray, B., 2023. Impact of lateral turbine spacing on the performance of a multi-rotor tidal energy device. Proc. Eur. Wave Tidal Energy Conf. http://dx.doi.org/10.36688/ewtec-2023-334.

Townley, B., Shi, W., Xiao, Q., Angeloudis, A., Ashton, I., Wray, B., 2025. Investigating the impact of multi-rotor structure shadowing on tidal stream turbine performance. Int. Mar. Energy J. 8 (2), 167–175. http://dx.doi.org/10.36688/imej.8.167-175.

White, F.M., 2006. Viscous Fluid Flow, third ed. New York, McGraw-Hill Higher Education.

Zahle, F., Sørensen, N.N., Johansen, J., 2009. Wind turbine rotor-tower interaction using an incompressible overset grid method. Wind. Energy 12 (6), 594–619. http://dx.doi.org/10.1002/we.327.